accepted for publication in IEEE Transactions on Medical Imaging, 2016

Spatially Variant Resolution Modelling for Iterative List-Mode PET Reconstruction

Matthew G. Bickell, Lin Zhou, Johan Nuyts

***Abstract*—A spatially variant resolution modelling technique is presented which estimates the system matrix on-the-fly during iterative list-mode reconstruction. This is achieved by redistributing the endpoints of each list-mode event according to derived probability density functions describing the detector response function and photon acollinearity, at each iteration during the reconstruction. Positron range is modelled using an image-based convolution. When applying this technique it is shown that the maximum-likelihood expectation maximisation (MLEM) algorithm is not compatible with an obvious acceleration strategy. The image space reconstruction algorithm (ISRA), however, after being adapted to a list-mode based implementation, is well-suited to the implementation of the model. A comparison of ISRA and MLEM is made to confirm that ISRA is a suitable alternative to MLEM. We demonstrate that this model agrees with measured point spread functions and we present results showing an improvement in resolution recovery, particularly for off-centre objects, as compared to commercially available software, as well as the standard technique of using a stationary Gaussian convolution to model the resolution, for equal iterations and only slightly higher computation time.**

***Index Terms*—Resolution modelling, detector response, photon acollinearity, positron range, block effect, system response, ISRA.**

I. Introduction

In positron emission tomography (PET) imaging accurately modelling the physical measurement process to account for the point spread function (PSF) can improve the subsequent resolution of the reconstruction [1]. In statistical reconstruction methods, such a model can be incorporated into the system matrix, which is a mapping between the detector elements and the voxels in the image space, and is referred to as resolution, or PSF, modelling. The state of the art in resolution modelling techniques has been summarised in [2].

In iterative reconstruction resolution modelling can be performed in the image domain or the projection domain. In the image domain a blurring kernel can be used to model the resolution. Reader *et al* [3] use a spatially invariant Gaussian kernel, which is simple to implement and produces images of high quality in terms of resolution recovery and noise reduction. Bowen *et al* [4] extend this technique by using a combination of a stationary Gaussian kernel and a radially varying kernel to model the spatially variant nature of the resolution. A set of measured point sources is used to determine the necessary kernel parameters. Similar techniques using different parameterisations of the PSF are presented in [5]–[7]. Projection domain techniques incorporate the system model directly into the system matrix. The system matrix can be measured (e.g. [8]), determined analytically (e.g. [9], [10]), or determined by Monte Carlo techniques (e.g. [11]–[13]). The propagation of errors in the system matrix through to the reconstructed image was studied by Qi *et al* [14].

In this paper, a spatially variant resolution modelling technique, which we reported on initially in [15] and refer to as the "Redistribution technique", is presented. In this model the dominant factors affecting the PSF, namely the detector response function, the acollinearity of the photon pair, and the positron range, are modelled for the Siemens microPET Focus220 small animal scanner (Preclinical Solutions, Siemens Healthcare Molecular Imaging, Knoxville, TN, USA). The model as derived in this paper can be applied to any ring scanner where the axial length is much less than the diameter; it can, however, be extended to other geometries. Probability density functions (PDFs) are derived which represent the statistical distribution of where the photons were absorbed in the detecting crystals. These PDFs are randomly sampled to redistribute the endpoints of each list-mode event, thereby distributing the events over the scanner field-of-view (FOV) in a way which is statistically more representative of the true photon flight paths, and hence modelling the system response. It is the intention to use this technique for list-mode based, event-by-event rigid motion correction. Sinogram-based motion correction approaches do exist, but these usually entail a significant loss in measured events [16], while a list-mode based approach is able to use all measured events which have corresponding motion information [17]. Therefore it was necessary to develop a list-mode technique which models the resolution in the projection domain, and does so for each individual event before it is motion corrected. For this application, it is computationally impractical to use a pre-calculated system matrix. Likewise, motion correction built into the reconstruction procedure is not generally amenable to spatially variant resolution modelling techniques operating in image space.

Similar techniques have been employed before in various ways to model the system matrix [10], [18]–[24]. Moehrs *et al* [18] used multiple integrations of lines of response associated with each detecting pair to determine the entire system matrix and use it within a sinogram-based MLEM reconstruction; Chen *et al* [19] used a multi-ray approach based on Monte Carlo techniques to construct a sensitivity image, and used

M. G. Bickell and J. Nuyts are with KU Leuven - University of Leuven, Department of Imaging and Pathology, Nuclear Medicine & Molecular imaging, Medical Imaging Research Center (MIRC), B-3000 Leuven, Belgium. L. Zhou was previously with the same group.

This work is supported by the IMIR project of KU Leuven and the MIRIAD Strategic Basic Research (SBO) project of the Innovatie door Wetenschap en Technologie (IWT).

this sensitivity image during simulated data reconstructions; Gillam *et al* [23] use a multi-ray technique to model the system matrix during MLEM reconstruction for an axial PET system, however they report that, to observe an improvement in resolution recovery, the method can be computationally expensive.

The approach which is presented in the current work models the system matrix on-the-fly without the need to perform a lengthy pre-calculation or storage of the system matrix, it uses very few and very simple point source measurements to fit one parameter, a multi-ray approach is approximated while only using each list-mode event once per iteration, and it produces a significantly enhanced resolution recovery for off-centre phantoms, with very similar noise levels to standard resolution modelling techniques. It is shown that, for our implementation, the MLEM algorithm may produce artefacts due to mathematical inconsistencies introduced when using an accelerated form of the list-mode based implementation. Therefore the use of the image space reconstruction algorithm (ISRA) [25] is recommended and demonstrated to avoid these mathematical inconsistencies.

II. Theory

The physical processes which contribute to a degradation of image resolution are: positron range, photon acollinearity, and the detector response function which incorporates the finite crystal stopping power, inter-crystal scattering of the photon, and imperfect scintillation light propagation through the light-guide to the photomultiplier tube (PMT) (i.e. the block effect). By analytically modelling these physical factors, suitable PDFs can be derived to describe the effect of each factor on the photon detection.

Each list mode event identifies a pair of photons detected by a particular detector pair (DP). The line which connects a predefined point on one detector to a similar point on the other at a predefined depth of interaction (DOI) along the centreline through the detectors is referred to as the line of response (LOR). This LOR is typically used in reconstructions without resolution modelling. The endpoints of the LOR can be redistributed according to the derived PDFs describing the physical factors affecting the resolution, thus creating one of infinitely many possible redistributed LORs (rLORs) associated with that DP. By repeating this redistribution many times for a single event, thus creating many rLORs, the true system matrix row for that DP can be sufficiently sampled. These redistributions can be performed during the reconstruction, thereby avoiding the need to precalculate and store the system matrix.

Since the scanner under consideration is the microPET Focus220 where the axial extent is much less than the scanner diameter, in the following sections the axial and transaxial components of the distributions are assumed to be separable. This is approximately true for all DPs except those which are very oblique, but these appear in the list-mode stream only rarely.

A. Photon acollinearity

If the annihilation location of the electron-positron pair were known exactly then either endpoint of the measured LOR could be shifted such that the resulting rLOR passes through the annihilation location. Since the annihilation location is not known, but rather the distribution of photon acollinearity angles, we can redistribute each endpoint of an LOR individually (while keeping the other fixed) many times according to this distribution to statistically represent the possible annihilation locations.

The distribution of the angular deviation of the photon pair acollinearity was measured by Colombino *et al* [26] and Trumpy [27], and described analytically as a sum of two Gaussians by Shibuya *et al* [28]. In [26] and [27] the line integral over the axial component of the acollinearity angle was measured, i.e.

$$Q(\phi_t) = C \int_{-\infty}^{\infty} \left(\frac{A_1}{\sqrt{2\pi}\sigma_1} e^{-\frac{\phi(\phi_t,\phi_z)^2}{2\sigma_1^2}} + \frac{1-A_1}{\sqrt{2\pi}\sigma_2} e^{-\frac{\phi(\phi_t,\phi_z)^2}{2\sigma_2^2}} \right) d\phi_z, \quad (1)$$

where the fit parameters are $A_1 = 0.791$, $\sigma_1 = 0.242°$, $\sigma_2 = 0.0695°$, C is a normalisation constant, and ϕ_t and ϕ_z are the transaxial and axial components of ϕ, respectively. Since ϕ is a small angle, it can be approximated by $\phi^2 = \phi_t^2 + \phi_z^2$. In our work we require the distribution at each angle of ϕ, i.e. only the integrand in (1), hence this integrand was used to model the acollinearity distribution.

An LOR which makes an angle of (θ_t, θ_z) with the normal to the detector surface in the transaxial and axial directions, respectively, can be redistributed by choosing a ϕ_t and ϕ_z according to the distribution given by the integrand of (1), as shown in figure 1. As a simplification we assume that the annihilation occurred midway between the detector surfaces. In the transaxial case, as shown in figure 1(a), by shifting one endpoint of the LOR by a small angle δ it can be suitably redistributed. This shift is given by

$$\delta = \arctan\left(\frac{D_t \sin\frac{\phi_t}{2}}{R\cos\left(\theta_t + \frac{\phi_t}{2}\right)} \right), \quad (2)$$

where R is the effective scanner radius taking the DOI into account, and D_t is transaxial distance between the LOR endpoints. By using a small angle approximation for ϕ_t we arrive at

$$\delta \simeq \arctan\phi_t \simeq \phi_t. \quad (3)$$

Similarly, in the axial direction, the spatial shift d along the detecting surface of an LOR endpoint (see figure 1(b)) is given by

$$d = \frac{D\sin\frac{\phi_z}{2}}{\cos\left(\theta_z + \frac{\phi_z}{2}\right)}, \quad (4)$$

where θ_z is the angle between the LOR and the normal to the detecting surface within the plane parallel to the axial

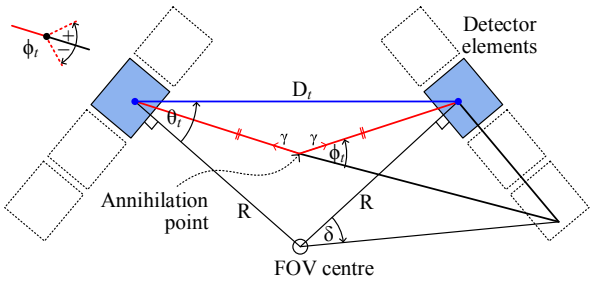

(a) The transaxial angle ϕ_t yields an angular shift δ.

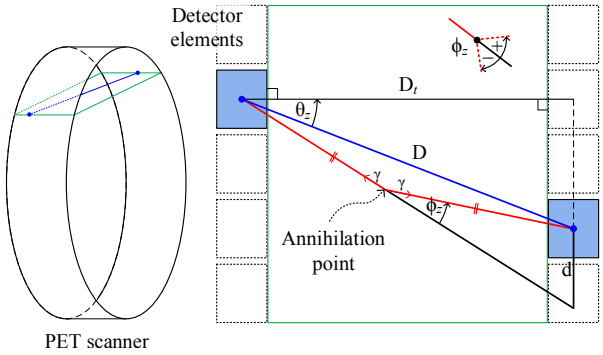

(b) The axial angle ϕ_z yields an spatial shift d.

Fig. 1. A diagram showing how an angle of acollinearity translates to a shift of one of the LOR endpoints. The flight path of the two photons is shown in red while the measured LOR is shown in blue. Only the photon acollinearity is being considered here, therefore the photon flight paths are assumed to terminate at the LOR endpoints. The detector response function is handled independently. The diagram is not to scale.

direction, and D is the distance between the LOR endpoints. Again making a small angle approximation, equation (4) simplifies to

$$d \simeq \frac{D^2 \phi_z}{2D_t}. \tag{5}$$

The rLOR is formed by redistributing one endpoint of the LOR, and selecting which endpoint at random. By repeating this procedure many times with different values of (ϕ_t, ϕ_z) for the same LOR, and backprojecting, the distribution of possible annihilation locations which could have resulted in that list-mode event being measured is approximated.

The above approach can be validated by comparing it to a theoretical distribution of the annihilation locations. Such a theoretical distribution can be determined for a given DP by calculating the probability that an annihilation in a particular voxel could have caused this DP to measure an event, resulting in an image-based PDF for the probability of a detection for each annihilation location. The comparison between the backprojection of the rLORs and the theoretical distributions is shown in figure 2. The central profile (midway between the DP) of the distribution from the rLORs matches that of the theoretical distribution. In the regions close to the endpoints the distribution is narrower than the theoretical prediction, which is due to the approximation that the annihilation event occurred on the line midway between the two detector surfaces. However, the distribution provides a reasonable approximation to the theoretical prediction.

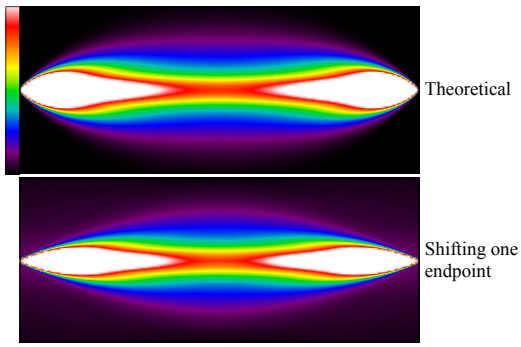

Fig. 2. Shown in the top frame is a 2D cross-section of the theoretical distribution of the possible annihilation location for a given LOR as a result of photon acollinearity. The resultant distribution using the proposed procedure, i.e. shifting each LOR endpoint individually many times, is shown in the lower frame. The vertical axis has been greatly exaggerated: actual spatial extents are 272 mm × 1.5 mm.

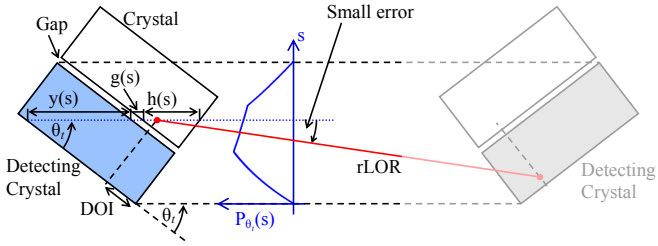

Fig. 3. The detector response function, $P_{\theta_t}(s)$, gives the probability that a photon with incident angle θ_t on the crystal surface will be detected at a distance s along the line perpendicular to the LOR. Each LOR endpoint is handled independently. This diagram is for the transaxial case; the axial case is the same except that the crystal surfaces are parallel.

B. *Detector response function*

The probability distribution of a photon being absorbed by one element of a DP when its trajectory is at a perpendicular distance, s, within the tube connecting the DP (see figure 3), can be approximated by

$$P_{\theta_t,\theta_z}(s) = \left(1 - e^{-\mu_c y(s)}\right) e^{-\mu_c h(s) - \mu_g g(s)}, \tag{6}$$

where $h(s)$ is the distance traversed in the neighbouring crystals, $y(s)$ is the total potential distance traversed in the crystal under consideration, $g(s)$ is the distance traversed through the gaps between the crystals, and μ_c and μ_g are the attenuation coefficients of the crystals and the material filling the gaps between the crystals, respectively, [9], [29], [30]. Equation (6) holds in both the transaxial and axial directions, and these two cases are assumed to be separable. The flight path of the photon is assumed to be parallel to the LOR. While this greatly simplifies the calculation of $y(s)$, $h(s)$ and $g(s)$, a small error is introduced since the resultant rLOR need not be parallel to the LOR (as shown in figure 3), but this error is negligible since the width of $P_{\theta_t}(s)$ is very small in comparison to the distance between the two detecting crystals.

In the transaxial direction, once a shift, s_t, has been randomly selected from the distribution in (6), the angular shift, δ', to be applied to the LOR endpoint under consideration

(similar to δ in figure 1(a)) is given by

$$\delta' = \arctan \frac{s_t}{R \cos \theta_t}, \tag{7}$$

where, as before, R is the effective scanner radius taking the DOI into account. In the axial direction the spatial shift, d', along the detecting surface for a given shift, s_z, is given by

$$d' = \frac{s_z}{\cos \theta_z}. \tag{8}$$

C. The block effect

For the scanner under consideration in this work, namely the Siemens microPET Focus220, the detecting elements are arranged in blocks of 12 crystals in a 42-sided polygon. This arrangement of the blocks is accounted for in the detector response function. Each detector block is attached to 4 photomultiplier tubes (PMTs). The so-called "block effect" contributes to resolution loss due to imperfect scintillation light propagation through the light-guide to the PMTs [31], [32]. This effect was modelled as suggested by [33] by allowing an LOR endpoint to be assigned to a neighbouring detecting element within the same block with a certain probability. This probability was determined empirically and is discussed in section VI-A.

D. Positron Range

The 2D projection of the positron range distribution can be modelled by

$$V(\rho) = Ae^{-\rho/B} + (1 - A)e^{-\rho/C}, \tag{9}$$

where ρ is the projected radial distance from the emission point and, for ^{18}F in water, $A = 0.851$, $B = 0.054$ mm and $C = 0.254$ mm, which were determined experimentally [1], [34]. For all of our studies, this isotope was used. A sinogram was constructed where each 2D projection was identical and given by equation (9) (since the positron range is isotropic). This sinogram was then reconstructed using a filtered backprojection to determine the 3D positron range distribution. The resulting 3D profile was sampled with a pixel size of 20 μm. A single hot pixel of the reconstruction pixel size was placed in a cold background and supersampled to match the pixel size of the positron range profile, by which it was then convolved. The resulting image was rebinned to the reconstruction pixel size to produce the final blurring kernel. This approach assumes that the radioactivity is uniformly distributed inside each pixel. The positron range was then incorporated into the resolution modelling by convolving the image by this blurring kernel before each projection and after each backprojection which used Redistribution.

III. Implementation

The endpoints of each recorded LOR are independently redistributed firstly according to the block effect, then the detector response function, and finally the acollinearity distribution, in both the transaxial and axial directions. These rLORs are then used in the reconstruction. During the reconstruction an image-space convolution is applied to model the positron range.

The system matrix can be denoted by a_{ij}, where i is the LOR index and j is the image voxel index. Let Ψ^i denote the infinite set of all possible rLORs associated with LOR i, and let $\psi \in \Psi^i$ be a random sample from the set of Ψ^i. Then the system matrix elements can be written as

$$s_i a_{ij} = s_i \lim_{R \to \infty} \frac{1}{R} \sum_r^R g^i_{\psi_r j} \simeq \frac{s_i}{R} \sum_r^R g^i_{\psi_r j}, \tag{10}$$

where $g^i_{\psi_r j}$ is the contribution of the rLOR ψ_r to the voxel j, and s_i is the combined normalisation coefficient (as determined during the system calibration) and the attenuation coefficient for LOR i. The infinite summation can be truncated to R terms to be computationally feasible. Each system matrix element, $g^i_{\psi_r j}$, is calculated using a ray-tracing algorithm.

The next two sections discuss how this system matrix was incorporated into two reconstruction algorithms. In the derivations and all experiments the additive contribution due to randoms and scatter was ignored.

A. List-mode MLEM with the Redistribution technique

The standard MLEM formulation, when applied to list-mode data [35], [36], is

$$\lambda_j^{n+1} = \frac{\lambda_j^n}{\sum_i^I s_i a_{ij}} \sum_m^M a_{i_m j} \frac{1}{\sum_k^J a_{i_m k} \lambda_k^n} \tag{11}$$

$$= \frac{\lambda_j^n}{\sum_i^I s_i a_{ij}} \sum_i^I \sum_\ell^{y_i} a_{ij} \frac{1}{\sum_k^J a_{ik} \lambda_k^n}, \tag{12}$$

where λ_j^n is the value of voxel j of the current reconstruction at iteration n, J is the number of voxels in the image, M is the number of measured events, the index i_m is the LOR associated with event m, I is the total number of possible LORs, and y_i is the number of times that LOR i appears in the list-mode data. Such a list-mode formulation allows for event-by-event motion correction [37]. Subsets can be utilised when implementing this algorithm, in which case it is referred to as the ordered-subsets expectation-maximisation (OSEM) algorithm [38]. When we incorporate the redistribution model, (10), into (12), we arrive at

$$\lambda_j^{n+1} = \frac{\lambda_j^n}{\frac{1}{R} \sum_i^I s_i \sum_r^R g^i_{\psi_r j}} \left(\sum_i^I \sum_\ell^{y_i} \sum_r^R g^i_{\psi'_r j} \frac{1}{\sum_k^J \sum_{r'}^R g^i_{\psi''_{r'} k} \lambda_k^n} \right), \tag{13}$$

where ψ'_r and ψ''_r are different for every ℓ to ensure that the modelling in the forward and backprojections are independent of each other. Since each LOR usually appears many times within the list-mode stream, i.e. $y_i > 1$, it is tempting to set $R = 1$ in the factor between the brackets and rely on the repetitions of each LOR to sample the system matrix sufficiently,

$$\lambda_j^{n+1} = \frac{\lambda_j^n}{\frac{1}{R} \sum_i^I s_i \sum_r^R g^i_{\psi_r j}} \left(\sum_i^I \sum_\ell^{y_i} g^i_{\psi'_\ell j} \frac{1}{\sum_k^J g^i_{\psi''_\ell k} \lambda_k^n} \right). \tag{14}$$

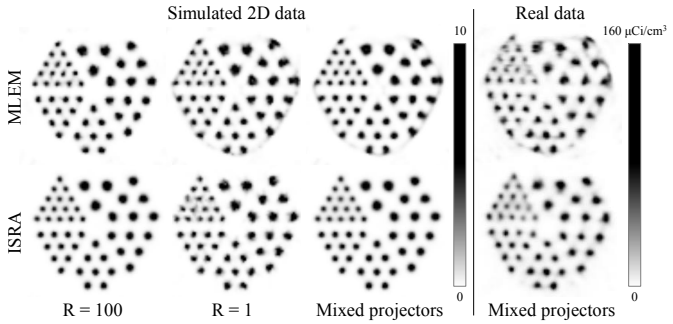

Fig. 4. Reconstructions of simulated 2D data with noise using 200 iterations and no subsets, and real data using 30 iterations and 9 subsets, for MLEM and ISRA. These data sets were obtained as described in sections V-B and V-C, respectively. To approximate the effect of scatter and randoms, a constant projection value for all possible LORs was added to the simulated data with total projection counts at 10% of those of the phantom; these were not corrected for in the reconstruction. In the third and fourth column the mixed projectors were used with $R = 1$. In the MLEM reconstructions with $R = 1$ (which includes the "Mixed projectors") artefacts can be observed along the edge of the phantom, while the corresponding ISRA reconstructions are artefact free.

This ensures that the implementation is computationally feasible since each list-mode event is only redistributed twice per iteration (once for the forward and once for the backprojection). At each iteration a new redistribution of the LORs is used, thereby further increasing the number of redistributed samples per LOR. However, it is immediately obvious that, with the summation over multiple instances of $g^i_{\psi''_\ell k}$ now occurring in the numerator, the system matrix element a_{ik} in the denominator is no longer approximated as defined by (10). By absorbing the summation over R into the summation over ℓ, we have essentially replaced a ratio of sums (sums over r and r' in (13)) with a sum of ratios (sum over ℓ in (14)). This is a very poor approximation which induces artefacts in the reconstruction. Reconstructions of simulated and real data when using the Redistribution technique with a large R and $R = 1$ are shown in figure 4. An artefact can be seen around the edge of the phantom which is due to the inaccurate approximation of a_{ik} as discussed above. Such artefacts tend to appear at the junction of high and low activity regions, specifically when rLORs which have very low projection values appear near to rLORs with much higher projection values. This artefact does not appear when R is large.

B. List-mode ISRA with the Redistribution technique

The structure of the image space reconstruction algorithm (ISRA) [25] is well suited to be used with this Redistribution technique since the forward and backprojection of the LORs both occur in the denominator. ISRA has the following sinogram-based formulation:

$$\lambda_j^{n+1} = \lambda_j^n \frac{\sum_i^I s_i a'_{ij} y_i}{\sum_i^I s_i^2 a'_{ij} \sum_k^J a_{ik} \lambda_k^n}, \tag{15}$$

where y is the measured sinogram. If the system matrix used for the backprojection is the same as that used for the forward projection, i.e. $a'_{ij} = a_{ij}$, then the algorithm is a non-negative unweighted least squares algorithm [39]. In [40] Reader *et al* discuss a generalised weighted least squares version of ISRA.

The formulation in (15) was adapted to be list-mode based. This was achieved by forward and backprojecting along all possible LORs in the denominator, which is equivalent to the sinogram-based approach except that no LORs were combined through mashing and spanning. The list-mode formulation can be written as

$$\lambda_j^{n+1} = \lambda_j^n \frac{\sum_m^M s_{i_m} a_{i_m j}}{\sum_i^I s_i^2 a_{ij} \sum_k^J a_{ik} \lambda_k^n}, \tag{16}$$

using the same definitions as in (11). Incorporating the redistribution model, (10), into (16) we obtain

$$\lambda_j^{n+1} = \lambda_j^n \frac{\sum_m^M s_{i_m} \sum_r^R g^{i_m}_{\psi_r j}}{\frac{1}{R} \sum_i^I s_i^2 \sum_r^R g^i_{\psi'_r j} \sum_k^J \sum_{r'}^R g^i_{\psi''_{r'} k} \lambda_k^n}. \tag{17}$$

To reduce the computational burden we can again set $R = 1$. In doing so we note that we now avoid the problem of approximating a ratio of sums with a sum of ratios, as was the case for MLEM. This is due to the fact that both the forward and backprojection of the current activity image estimate occur in the denominator. As can be seen in figure 4, ISRA does not produce any reconstruction artefacts when $R = 1$. As before, at each iteration a new redistribution is performed, thereby increasing the number of samples of the distributions.

C. Noise reduction using mixed projectors

To ensure that the implementation of the technique is computationally feasible, it is preferable to use $R = 1$. Therefore it is necessary to use ISRA instead of MLEM. However, as can be seen in figure 4, a significant amount of noise is introduced into the reconstructions when $R = 1$ due to the random nature of the Redistribution technique. In the standard image-based resolution modelling technique [3], a smoothing operator is applied to the image before forward projection and after backprojection. We explored replacing the redistribution in the backprojection by a similar smoothing operator which matched the PSF in the FOV centre. By performing this smoothing operation the noise introduced by the Redistribution technique is suppressed while still maintaining the accurate model for the resolution during the forward projection.

Other authors have successfully applied unmatched projectors, for example [41]. We have found empirically that the proposed algorithm converges, but have not yet been able to definitively prove it.

Using these projectors, the MLEM algorithm can then be

TABLE I
NOISE LEVELS USED FOR THE 2D SIMULATIONS.

Noise level	High	Medium	Low
Total counts ($\times 10^6$)	1.12	3.36	6.73
Mean of non-zero counts	84.0	263.4	523.5

formulated as

$$\lambda_j^{n+1} = \frac{\lambda_j^n}{\sum_\xi^\Xi G_{j\xi} \sum_i^I s_i g_{0\xi}^i} \left(\sum_\xi^\Xi G_{j\xi} \sum_i^I \sum_\ell^{y_i} g_{0\xi}^i \times \frac{1}{\frac{1}{R} \sum_k^J \sum_r^R g_{\psi_r'' k}^i \lambda_k^n} \right), \tag{18}$$

where $g_{0\xi}^i$ is the unredistributed LOR i and G is a Gaussian convolution kernel containing Ξ elements per voxel. For the microPET Focus220 the FWHM of this Gaussian kernel is 1.3 mm in all 3 directions [42]. For ISRA we obtain the following implementation

$$\lambda_j^{n+1} = \lambda_j^n \frac{\sum_\xi^\Xi G_{j\xi} \sum_m^M s_{i_m} g_{0\xi}^{i_m}}{\frac{1}{R} \sum_\xi^\Xi G_{j\xi} \sum_i^I s_i^2 g_{0\xi}^i \sum_k^J \sum_r^R g_{\psi_r k}^i \lambda_k^n}. \tag{19}$$

The results of this implementation with $R = 1$ are shown in figure 4, labelled as "Mixed projectors". For both MLEM and ISRA the noise is greatly reduced, however, for MLEM, the artefact is still present. Hence, in this work we made use of ISRA with $R = 1$ and the mixed projectors.

IV. COMPARING MLEM AND ISRA

To further justify the use of ISRA instead of MLEM, a short comparison of the two algorithms was performed. In MLEM the noise is modelled as a Poisson distribution, which is not true for ISRA, and constitutes a significant advantage of MLEM over ISRA. Reader *et al* compared the performance of MLEM and ISRA in [40] for a sinogram-based implementation. We conduct a similar investigation here and also include a list-mode implementation, which is of interest in the current context. Two dimensional simulations were conducted for 100 noise realisations at three noise levels, and the bias and standard deviation of OSEM and ordered subsets (OS) ISRA reconstructions were compared. Since it is not computationally feasible to use the Redistribution technique with a large R for MLEM, and to avoid confounding factors by using the Redistribution technique, for both algorithms the resolution was modelled using the standard Gaussian convolution in image space. The properties of the three noise levels are summarised in table I.

The absolute difference bias and standard deviation were calculated as follows:

$$b^k = \frac{1}{P} \sum_j^P \left| \bar{\lambda}_j^k - t_j \right|, \tag{20}$$

$$\sigma^k = \sqrt{\frac{1}{NP-1} \sum_j^P \sum_n^N \left(\lambda_{jn}^k - \bar{\lambda}_j^k \right)^2}, \tag{21}$$

where $\bar{\lambda}_j^k$ is the j^{th} pixel of the average reconstruction over all noise realisations at iteration k, P is the number of pixels in the region-of-interest (ROI), t_j is the ground truth image, and λ_{jn}^k is the reconstruction of the noisy data at iteration k for noise realisation n, of which there are N. MLEM will rapidly reconstruct the support of the phantom in a cold background, while ISRA, being an unweighted least squares optimiser, will do so much more slowly. As a result, the bias of MLEM was observed to be significantly lower than that of ISRA at the boundary of the reconstructed object. Assuming that for most applications the exact reconstruction of the boundary is not as important as the intensities inside the support of the object, we chose to analyse the bias and standard deviation in a ROI which was obtained by eroding the object support by 2 pixels. Bias and standard deviation images were calculated using

$$B_j^k = \bar{\lambda}_j^k - t_j, \tag{22}$$

$$S_j^k = \sqrt{\frac{1}{N-1} \sum_n^N \left(\lambda_{jn}^k - \bar{\lambda}_j^k \right)^2}. \tag{23}$$

A. Sinogram implementation with subsets

As can be seen in figure 5, the standard deviation and bias of the sinogram-based OSEM and OS-ISRA are similar for all iterations. See also the bias and standard deviation images in figure 6 where the efficacy of OSEM at reconstructing the object support can be seen in comparison to OS-ISRA, and an example reconstruction in figure 8.

B. List-mode implementation with subsets

In the list-mode case, if subsets are to be used to accelerate the reconstructions, certain approximations need to be made for both OSEM and OS-ISRA. In OSEM the backprojection of the sensitivity sinogram is over all possible LORs. In a sinogram-based implementation the backprojection can be computed independently for each subset to match the projections of the measured data [38], but in a list-mode implementation this is not easy since the events in the list-mode stream are in no particular order. In OS-ISRA [43], a similar argument applies: the measured data, which are backprojected in the numerator of (16), can not easily be divided into subsets to match the projections in the denominator. For this reason, in OSEM the backprojection of the entire sensitivity sinogram is simply scaled by the number of subsets, as is the backprojection of all the measured data in OS-ISRA. It is then assumed that each subset of the events used in the projections will be sufficiently statistically representative of the entire set to match the scaled backprojections. After each iteration the events are randomly shuffled to ensure that the subsets are never identical from one iteration to the next.

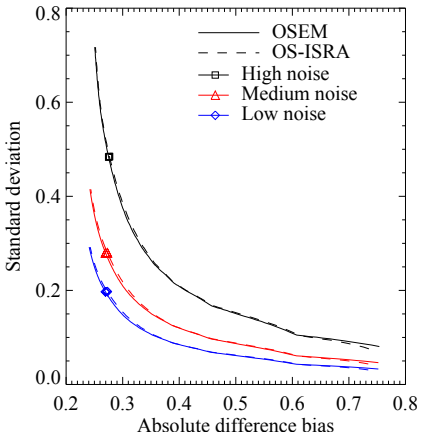

Fig. 5. A bias versus standard deviation plot for a sinogram implementation of OSEM and OS-ISRA for 3 noise levels and 100 noise. Reconstructions were performed using 25 iterations and 21 subsets. In these plots the iterations are increasing with increasing standard deviation. The small symbols indicate where the end of iteration 12 lies.

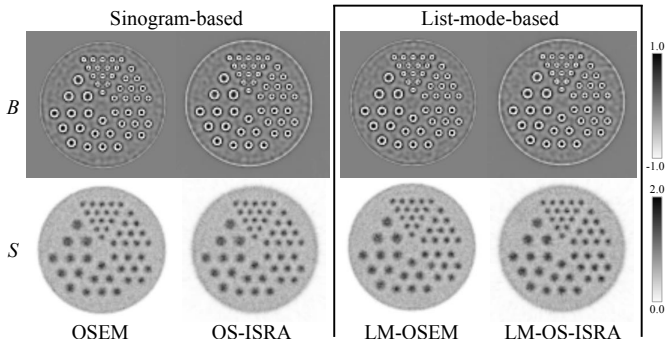

Fig. 6. The bias and standard deviation images at the last iteration for the high noise case.

Figure 7 shows the standard deviation versus bias results for the list-mode reconstructions, with the corresponding images in figure 6 and an example reconstruction in figure 8. While OS-ISRA exhibits a higher standard deviation than OSEM in earlier iterations, it converges to a result similar to that of OSEM. For matched biases though OS-ISRA does have a higher standard deviation.

C. Discussion

In [40] Reader *et al* found that sinogram-based ISRA and MLEM converge to similar quantitative values, as we conclude here. Their results on the mean absolute error, which is similar to our definition of the absolute bias (20), demonstrate that, while ISRA converges more slowly, it reaches quantitative values similar to that of MLEM within the support of the object.

In the sinogram case OSEM and OS-ISRA produce similar bias-standard deviation curves. This was also verified in the list-mode case when no subsets are used (results not presented here). However, when subsets are introduced the standard deviation of list-mode OS-ISRA increases. In the denominator of the list-mode ISRA equation (16), each LOR which passes through the reconstruction image space is used once per iteration. In list-mode MLEM (11), however, all the measured

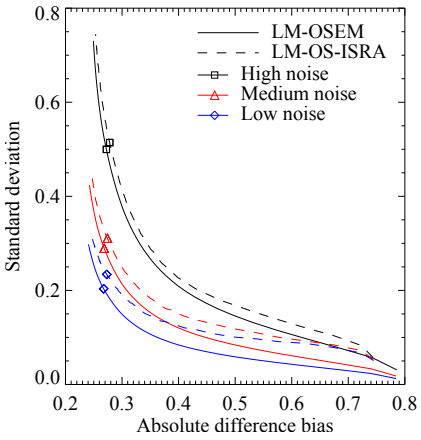

Fig. 7. A bias versus standard deviation plot for a list-mode implementation of OSEM and OS-ISRA for 3 noise levels and 100 noise realisations. Only the points at the end of each iteration are plotted. Reconstructions were performed using 105 iterations and 5 subsets. The iteration number is increasing with increasing standard deviation, and the small symbols indicate where the end of iteration 52 lies.

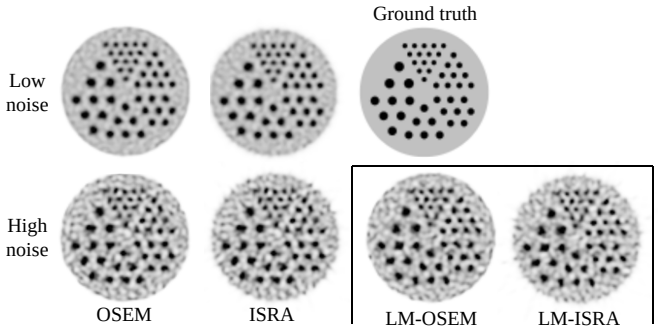

Fig. 8. On the left are the sinogram-based reconstructions using 21 subsets of the high and low noise data after 12 complete iterations of a single noise realisation. On the lower right are the list-mode reconstruction using 5 subsets after 52 complete iterations of the high noise case. The ground truth is also shown for reference. All images are shown to the same scale.

events are used in each iteration. In the 2D case considered here, for the microPET Focus220, there are several million measured list-mode events while only 20000 LORs passing through the image space. Therefore OS-ISRA uses far fewer projections per subset than OSEM, leading to a significantly reduced computation time (by a factor of 50 in the high noise case, and more in the others). However, each subset in OS-ISRA may introduce significantly more noise than those in OSEM, leading to an increased standard deviation in the reconstructions, as can be seen in figure 7. In the real 3D case the OS-ISRA computation time and noise propagation will be more similar to those of OSEM since the number of possible LORs is then on the same order of magnitude as the number of measured list-mode events; this was not fully investigated though.

Nonetheless, we assert that the potential gain in using ISRA with the Redistribution technique to achieve spatially variant resolution modelling (as demonstrated below) may outweigh the noise-performance differences observed between the two algorithms.

V. Experiments

For all experiments and simulations the Siemens microPET Focus220 small animal scanner was used and modelled. This scanner has an internal diameter of 258 mm, and a spatial resolution of 1.3 mm at the centre of the FOV. At a radial distance of 60 mm the spatial resolution degrades to $[1.9, 2.1, 3.2]$ mm in the tangential, axial, and radial components respectively [42].

A. Spatially variant nature verification

To investigate the spatially variant nature of the Redistribution technique, a point source was measured within the microPET scanner. The point source was a porous microsieve with a diameter of 2.1 mm and was placed inside putty to provide a uniform surrounding material. For each measurement the centre-of-mass position of the point source was determined from a reconstruction of the data, and a point source of the same size was then simulated in that position. The point source was convolved with the positron range kernel described in section II-D. Two forward projection models were used to create simulated sinograms:

A The resolution was modelled by convolving the image with a spatially invariant Gaussian kernel with FWHM = 1.3 mm. The resulting image was then forward projected to sinogram space.

B The resolution was modelled with the proposed technique: a forward projection was performed using the system matrix elements given in equation (10) with $R = 500$, and the projection values were binned into a sinogram.

The resulting sinograms were compared to the measured sinogram to determine the accuracy of each model in estimating the PSF.

B. Simulations

Two 2D phantoms were simulated: a hot-rod phantom of diameter 40 mm and with rods of diameter $1.5 - 3.0$ mm, similar to the one used in our experiments, and a Shepp-Logan phantom. The total activity in the Shepp-Logan phantom was 6 times that in the hot-rod phantom. These were placed 54 mm off-centre of the scanner FOV and used to simulate list-mode data. A comparison was made of ISRA reconstructions using no resolution modelling, the standard Gaussian convolution model with FWHM = 1.3 mm, and the Redistribution technique. One hundred iterations with no subsets, using a pixel size of 0.4745 mm in both directions, were used for the reconstructions.

For these simulations the so-called "inverse crime" was committed: to model the physics during the generation of the list-mode data the Redistribution technique was used during the forward projection of the ground truth, with $R = 500$ (however, a different seed was used to generate the random numbers used during the reconstruction). A Poisson realisation of the projection values was made to yield the expected count rates; these could then be used to create the list-mode data. The data was randomised and time stamps were assigned to each list-mode event.

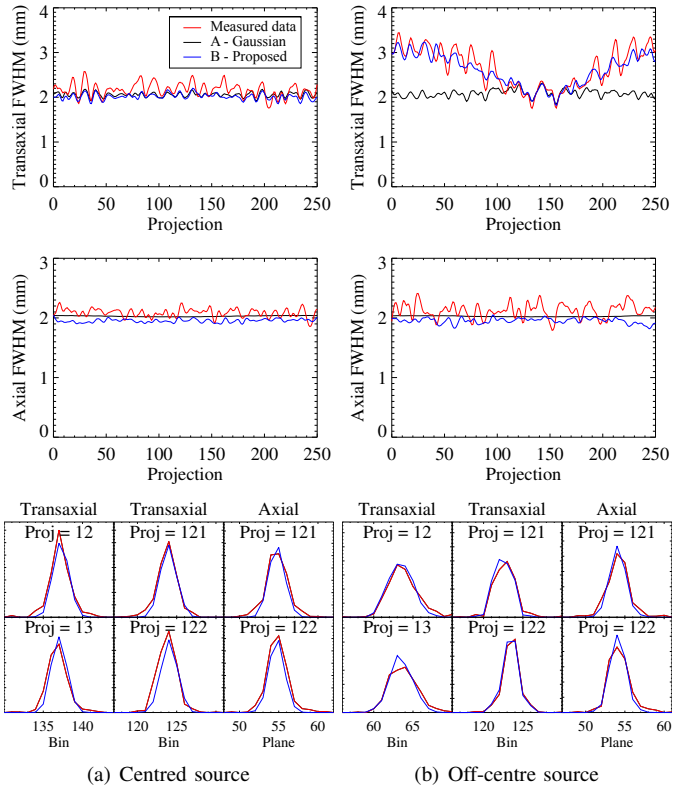

(a) Centred source (b) Off-centre source

Fig. 9. The FWHMs in the transaxial and axial directions as a function of projection index in the measured sinogram and the sinogram produced when using the models described in section V-A. In the left column the point source was located 16.9 mm transaxially from the centre of the FOV, and in the right column the point source was at a transaxial distance of 65.1 mm; both sources were at an axial distance of 6.0 mm from the FOV centre. The FWHM plots have been smoothed, and the sinograms were not deconvolved by the size of the point source before calculating these FWHMs. The profiles through the measured and the proposed model sinograms are also shown below.

C. Real data

A hot-rod phantom of diameter 40 mm and with rods of diameter $1.5 - 3.0$ mm was scanned in the microPET scanner. The phantom was filled with between $1.0 - 1.5$ mCi of FDG and scanned for 2 minutes in the centre of the scanner, 5 minutes at a radial distance of 35 mm horizontally to the right of the FOV centre, and again for 5 minutes at a radial distance of 54 mm. The data were reconstructed with OS-ISRA using the Redistribution technique, and compared to reconstructions with OSEM using the standard Gaussian convolution technique, as well as a commercial maximum a-posteriori (MAP) OSEM reconstruction algorithm by Siemens. The OS-ISRA and OSEM reconstructions were performed using 20 iterations and 9 subsets, and the MAP-OSEM reconstruction used 2 OSEM iterations and 9 subsets followed by 18 MAP iterations, with a target resolution of 0.5 mm and enforcing uniform resolution. The MAP-OSEM algorithm models the resolution using PSF tables based on point source measurements for this particular scanner. The pixel size of all reconstructions was $[0.4745, 0.4745, 0.796]$ mm.

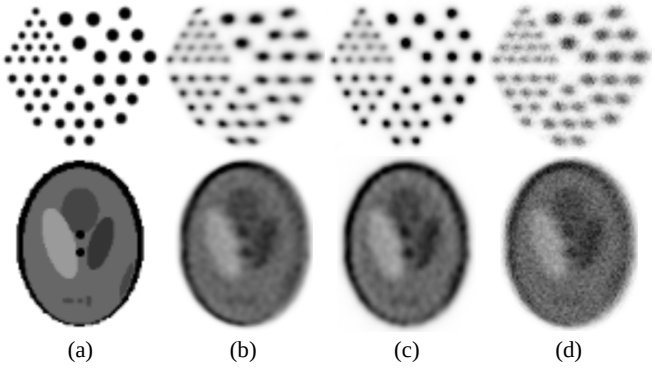

Fig. 10. Results from 2D simulations using different resolution modelling techniques for two phantoms: (a) the ground truth; (b) using the standard Gaussian convolution model; (c) using the Redistribution technique; (d) no resolution modelling. The phantoms were placed to the right of the centre of the scanner FOV. For each phantom, all images are shown to the same scale.

VI. Results

A. Spatially variant nature verification

By minimising the difference between the profiles of the measured and simulated sinograms for various point source locations and block effect parameters, the probability parameter for the modelling of the block effect was empirically set. It was determined that an LOR endpoint should be redistributed to a neighbouring detector crystal with a probability of $\frac{N}{64}$, where N is the number of neighbours: 8 for endpoints within the block, 5 for those at the edge of the block, and 3 for those at a corner. Tomic *et al* [32] found a similarly small probability for a block detector of a different scanner.

Figure 9 shows a comparison of the FWHM of each projection index of the simulated sinograms with those of the measured data. To reduce the effect of noise in all sinograms, in the transaxial case the three planes immediately about the maximal plane were summed before calculating the FWHM for each projection. Similarly, in the axial case the three projection values immediately about the maximal value were summed.

For a point source located near the centre of the FOV the FWHMs of the projections are quite constant, as expected. However, for transaxially off-centre point sources the FWHMs of the measured data vary with the projection angle, and this behaviour is accurately modelled by the Redistribution technique. Since the Gaussian convolution is spatially invariant, the FWHMs are not affected by the point source position and it thus underestimates the FWHM of the PSF for angles where the projection of the point source is off-centre.

B. Simulations

The results from the simulations are shown in figure 10. In the case of the hot-rod phantom, since the phantom is off-centre, the Gaussian convolution technique has underestimated the width of the PSF and distorted the rods away from the centre. On the other hand, the Redistribution technique has preserved the circular shape of the rods. A similar effect can be seen at the edge of the Shepp-Logan phantom.

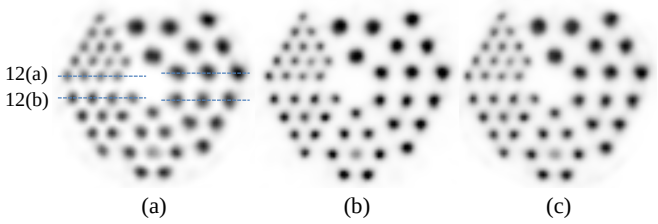

Fig. 11. Reconstructions of the centred phantom: (a) reconstruction using the standard Siemens software (a MAP-OSEM algorithm); (b) using OS-ISRA and the Redistribution technique; (c) using OSEM and the standard Gaussian convolution model. All images are shown to the same scale. Note that the smallest rod closest to the centre had an air pocket and did not contain any activity during the scan. The ground truth of this phantom is shown in figure 10(a).

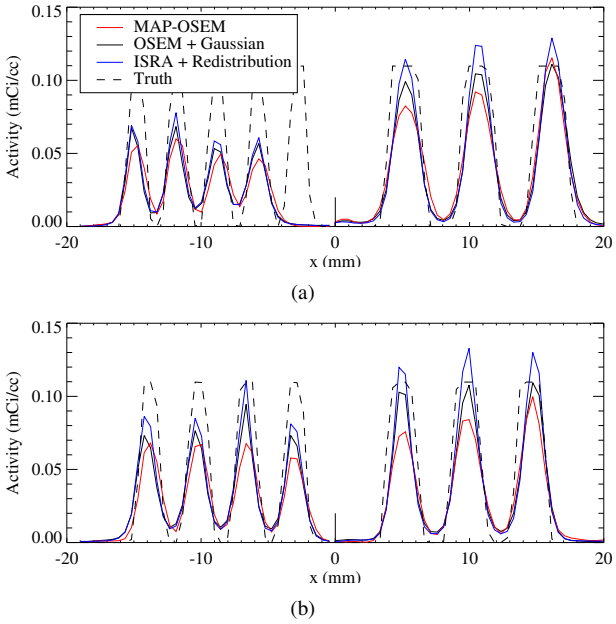

Fig. 12. Profiles through the reconstructions shown in figure 11, as indicated in figure 11(a).

Even though the inverse crime is committed here, these results demonstrate that the method works well under ideal conditions, and also demonstrates the effect of using the stationary Gaussian convolution model on data with a spatially variant PSF.

C. Real data

The reconstructions of the centred phantom are shown in figure 11 with two profiles through the reconstructions shown in figure 12. The ground truth image was created and scaled to have the same total activity as the Siemens reconstruction, and the total activities in all reconstructions are equal to within 4%. All three algorithms have produced very similar reconstructions with regards to resolution recovery, as expected for a phantom near the FOV centre.

Figure 13 shows the reconstruction of the off-centre phantom at 35 mm from the centre. The total activity of the reconstructions agree to within 3%. The resolution recovery of the Redistribution and Gaussian techniques is superior to

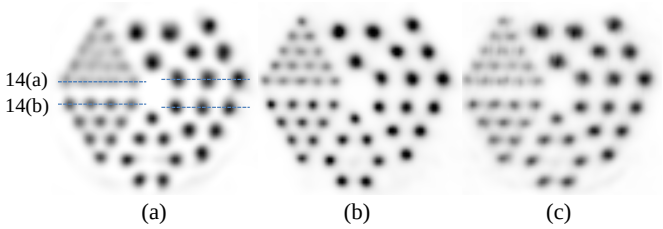

Fig. 13. Reconstructions of the off-centre phantom (positioned 35 mm to the right of the FOV centre): (a) reconstruction using the standard Siemens software (a MAP-OSEM algorithm); (b) using OS-ISRA and the Redistribution technique; (c) using OSEM and the standard Gaussian convolution model. All images are shown to the same scale. By comparing the smallest rods, one can see that the resolution recovery of (b) and (c) is superior to that of (a).

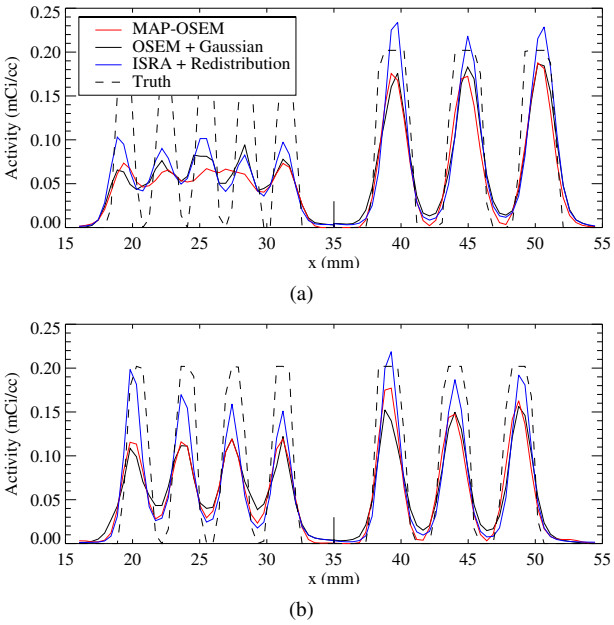

Fig. 14. Profiles through the reconstructions shown in figure 13, as indicated in figure 13(a).

the MAP-OSEM reconstruction, as can be seen by comparing the smallest rods. However the Redistribution technique and MAP-OSEM algorithm have produced less rod distortion than the Gaussian technique. From figure 14 it can be seen that, of the three reconstructions, the Redistribution technique has produced the best resolution recovery.

The reconstructions of the second off-centre phantom at 54 mm from the centre are shown in figures 15 and two profiles in figures 16. Due to limitations in the commercial software, it was not possible to reconstruct this data using the Siemens MAP-OSEM algorithm since the phantom was outside the reconstructable volume. For comparison's sake, the data was reconstructed using OSEM without any resolution modelling. The total activity of the reconstructions are equal to within 1.5%, and the OS-ISRA reconstruction was used to scale the ground truth image. The Redistribution technique has produced a reconstruction with a superior resolution recovery to the Gaussian convolution model, as can be seen in figure 16. It has also preserved the circular shape of the rods while the Gaussian model has distorted them away from

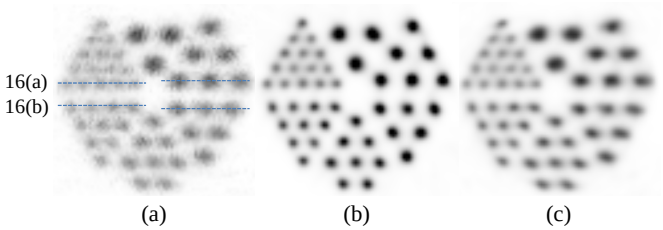

Fig. 15. Reconstructions of the off-centre phantom (positioned 54 mm to the right of the FOV centre): (a) reconstruction using OSEM without any resolution modelling; (b) using OS-ISRA and the Redistribution technique; (c) using OSEM and the standard Gaussian convolution model. All images are shown to the same scale. Note that the circular shape of the rods has been preserved in (b) but have been distorted away from the FOV centre (i.e. to the right) in (c).

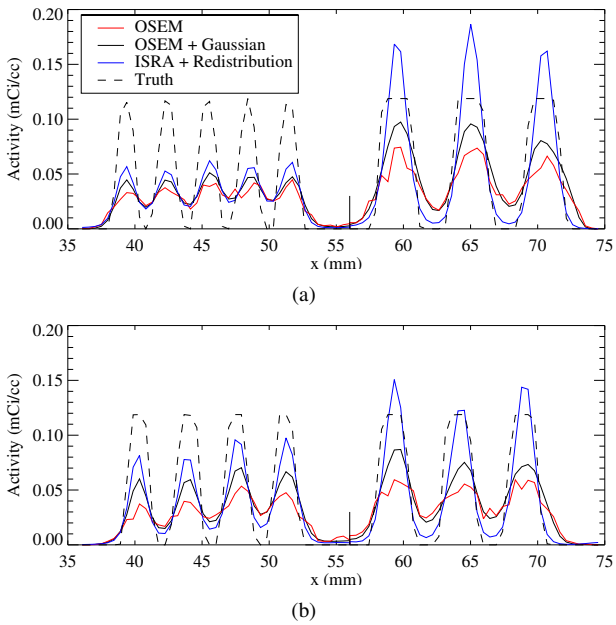

Fig. 16. Profiles through the reconstructions shown in figure 15, as indicated in figure 15(a).

the FOV centre (i.e. to the right). Both models have produced better resolution recovery than the reconstruction without any resolution modelling, as expected.

VII. Discussion

The accuracy of the spatially variant nature of the resolution model using the Redistribution technique was verified by using it as a forward projection model and comparing it to measured data. The FWHMs of the resultant projections in the sinograms matched those of the measured data, for centred and off-centre locations in the FOV.

Using this result, the Redistribution technique was used as a forward projection model in 2D phantom simulations, and the results demonstrated that, for off-centre phantoms, the Redistribution technique produces reconstructions which preserve the true shape of the phantom, while the spatially invariant Gaussian convolution technique distorts the activity away from the centre.

Reconstructions of real data demonstrated that OS-ISRA with the Redistribution technique, OSEM with the Gaussian

convolution technique, and the Siemens MAP-OSEM algorithm all produce very similar results for centred phantoms, which is expected since all algorithms provide a good approximation to the resolution of the system near the centre of the FOV. For off-centre phantoms, however, the Redistribution technique produces superior resolution recovery which matches the ground truth quite well and preserves the shape of the phantom, while the Gaussian convolution technique distorts the phantom away from the FOV centre. This effect becomes more pronounced with increasing radial distance.

The Redistribution technique has caused overshoot to occur on some of the rods, as can be seen in figure 16. This is due to the Gibbs effect, which can produce pronounced results in small structures [44].

The projectors used for the in-house reconstructions were ray-tracing projectors and since the pixel size was usually smaller than the detector cell size, the known artefacts associated with these projectors were observed [45], as can be seen in figure 15(a). The distance-driven projector is known to solve this issue, however it is not easy to implement for list-mode data. It is interesting to note that both the Gaussian convolution and the Redistribution techniques have removed these artefacts.

Since a list-mode implementation of OSEM and OS-ISRA has been used, a direct comparison of the number of computations per iteration is not straightforward. For OSEM, the number of forward and backprojections in one iteration is exactly the number of measured list-mode events. Whereas in OS-ISRA, the measured data are backprojected once before the reconstruction begins, and then a list of all possible LORs which pass through the reconstruction image space is generated and these LORs are forward and backprojected in each iteration. Therefore, for OSEM, the number of computations per iterations is proportional to the number of measured events, while for OS-ISRA this number depends on the size and location of the image space. As an indication though, for a centred phantom filled with approximately 1 mCi of FDG and scanned for 2 minutes in the microPET Focus220 scanner, approximately 55 million events were recorded, which is approximately the same number of possible LORs which pass through a centred image space of size $[61.0, 61.0, 76.0]$ mm (the image space used for the reconstructions in figure 11). The reconstruction of this data in this image space takes about 35% more time for an OS-ISRA reconstruction with Redistribution than for an OSEM reconstruction with the Gaussian convolution.

For a small animal scanner such as the microPET Focus220, the effect of photon acollinearity on the spatial resolution is very small. Also, for ^{18}F, the effect of the positron range is very small. Nonetheless both these effects were modelled in the presented work for the sake of generality, and to allow for an easy conversion to clinical scanners, and other isotopes, where these effects are more pronounced. The positron range was modelled in a spatially invariant manner; we will adapt this in the future to be more physically realistic.

Since the Redistribution technique models the resolution during the projections, and not in image-space, it is well-suited to be used in conjunction with event-by-event list-mode rigid motion correction. The LORs can be redistributed before being motion corrected, and then used in the reconstruction, thus accurately modelling the spatial variance of the system response. This approach is beyond the scope this report and will be implemented in future work.

VIII. Conclusion

The Redistribution technique, a resolution modelling technique which models the system response on-the-fly during iterative reconstruction, has been presented. The system response is described analytically using PDFs which are sampled to redistribute the endpoints of the LORs used during the reconstruction. By adjusting the endpoints of the LORs in this way, a system matrix is estimated which varies radially, axially and transaxially. We found that the proposed geometric model accurately captures the spatial variance of the system resolution of the microPET Focus220. The only parameter that was tuned based on measurements is the one modelling the "block effect", i.e. the cross-talk between crystals. Once this parameter was determined, the model was found to agree very well with all projections of point sources placed at different positions in the scanner.

It was demonstrated that the formulation of the MLEM algorithm is not well-suited to use the Redistribution technique in a computationally feasible implementation, and so the ISRA algorithm was used as an alternative.

A comparison of phantom reconstructions using standard Siemens software (a MAP-OSEM algorithm), the OSEM algorithm with and without resolution modelling using a stationary Gaussian convolution, and the OS-ISRA algorithm with the Redistribution technique demonstrated that all the algorithms produce very similar reconstructions for phantoms near the centre of the scanner FOV, as expected, while the presented technique produces reconstructions with superior resolution recovery for off-centre phantoms. The Redistribution technique accurately preserves the shape of the imaged object and does not distort the reconstructions away from the centre, as a spatially invariant technique does.

References

[1] S. E. Derenzo, "Mathematical Removal of Positron Range Blurring in High Resolution Tomography," *IEEE Trans. Nucl. Sci.*, vol. 33, no. 1, pp. 565–569, 1986.

[2] A. Rahmim, J. Qi, and V. Sossi, "Resolution modeling in PET imaging: theory, practice, benefits, and pitfalls." *Med. Phys.*, vol. 40, no. 6, p. 064301, Jun. 2013.

[3] A. Reader, P. Julyan, H. Williams, D. Hastings, and J. Zweit, "EM Algorithm System Modeling by Image-Space Techniques for PET Reconstruction," *IEEE Trans. Nucl. Sci.*, vol. 50, no. 5, pp. 1392–1397, Oct. 2003.

[4] S. L. Bowen, L. G. Byars, C. J. Michel, D. B. Chonde, and C. Catana, "Influence of the partial volume correction method on (18)F-fluorodeoxyglucose brain kinetic modelling from dynamic PET images reconstructed with resolution model based OSEM." *Phys. Med. Biol.*, vol. 58, no. 20, pp. 7081–106, 2013.

[5] A. Rahmim, M. Lenox, C. Michel, A. Reader, and V. Sossi, "Space-variant and anisotropic resolution modeling in list-mode EM reconstruction," *IEEE Nucl. Sci. Symp. Conf. Rec.*, no. 1, pp. 3074–3077, 2004.

[6] E. Rapisarda, V. Bettinardi, K. Thielemans, and M. Gilardi, "Image-based point spread function implementation in a fully 3D OSEM reconstruction algorithm for PET," *Phys. Med. Biol.*, vol. 55, pp. 4131–4151, 2010.

[7] C. Cloquet, F. C. Sureau, M. Defrise, G. Van Simaeys, N. Trotta, and S. Goldman, "Non-Gaussian space-variant resolution modelling for list-mode reconstruction." *Phys. Med. Biol.*, vol. 55, no. 17, pp. 5045–5066, 2010.

[8] V. Y. Panin, F. Kehren, C. Michel, and M. Casey, "Fully 3-D PET reconstruction with system matrix derived from point source measurements," *IEEE Trans. Med. Imaging*, vol. 25, no. 7, pp. 907–21, Jul. 2006.

[9] R. Lecomte, D. Schmitt, and G. Lamoureux, "Geometry Study of a High Resolution PET Detection System Using Small Detectors," *IEEE Trans. Nucl. Sci.*, vol. NS-31, no. 1, pp. 556–561, 1984.

[10] R. H. Huesman, G. J. Klein, W. W. Moses, J. Qi, B. W. Reutter, and P. R. Virador, "List-mode maximum-likelihood reconstruction applied to positron emission mammography (PEM) with irregular sampling." *IEEE Trans. Med. Imaging*, vol. 19, no. 5, pp. 532–7, May 2000.

[11] E. Mumcuoglu and R. Leahy, "Accurate geometric and physical response modelling for statistical image reconstruction in high resolution PET," *IEEE*, pp. 1569–1573, 1996.

[12] J. Qi, R. M. Leahy, S. R. Cherry, A. Chatziioannou, and T. H. Farquhar, "High-resolution 3D Bayesian image reconstruction using the microPET small-animal scanner," *Phys. Med. Biol.*, vol. 43, no. 4, pp. 1001–13, Apr. 1998.

[13] R. Yao, R. M. Ramachandra, N. Mahajan, V. Rathod, N. Gunasekar, A. Panse, T. Ma, Y. Jian, J. Yan, and R. E. Carson, "Assessment of a three-dimensional line-of-response probability density function system matrix for PET." *Phys. Med. Biol.*, vol. 57, no. 21, pp. 6827–48, Nov. 2012.

[14] J. Qi and R. H. Huesman, "Effect of errors in the system matrix on maximum a posteriori image reconstruction." *Phys. Med. Biol.*, vol. 50, no. 14, pp. 3297–3312, 2005.

[15] M. G. Bickell, L. Zhou, and J. Nuyts, "Spatially Variant Resolution Modelling for Iterative List-Mode PET Reconstruction," *IEEE Nucl. Sci. Symp. Conf. Rec.*, 2013.

[16] P. M. Bloomfield, T. J. Spinks, J. Reed, L. Schnorr, A. M. Westrip, L. Livieratos, R. Fulton, and T. Jones, "The design and implementation of a motion correction scheme for neurological PET." *Phys. Med. Biol.*, vol. 48, no. 8, pp. 959–978, 2003.

[17] A. Z. Kyme, V. W. Zhou, S. R. Meikle, and R. R. Fulton, "Real-time 3D motion tracking for small animal brain PET," *Phys. Med. Biol.*, vol. 53, pp. 2651–2666, 2008.

[18] S. Moehrs, M. Defrise, N. Belcari, A. D. Guerra, A. Bartoli, S. Fabbri, and G. Zanetti, "Multi-ray-based system matrix generation for 3D PET reconstruction," *Phys. Med. Biol.*, vol. 53, no. 23, pp. 6925–45, Dec. 2008.

[19] Y. Chen and S. J. Glick, "Determination of the System Matrix Used in List-Mode EM Reconstruction of PET," *IEEE Nucl. Sci. Symp. Conf. Rec.*, pp. 3855–3858, 2007.

[20] M. G. Bickell, A. Buffler, and I. Govender, "A fully 4D mesh parameterisation PET image reconstruction algorithm for list-mode data," *IEEE Nucl. Sci. Symp. Conf. Rec.*, pp. 2620–2624, Oct. 2011.

[21] E. Gonzalez, J.-y. Cui, and G. Pratx, "Point spread function for PET detectors based on the probability density function of the line segment," *IEEE Nucl. Sci. Symp. Conf. Rec.*, pp. 4386–4389, 2011.

[22] X. Jin, C. Chan, T. Mulnix, V. Panin, M. E. Casey, C. Liu, and R. E. Carson, "List-mode reconstruction for the Biograph mCT with physics modeling and event-by-event motion correction," *Phys. Med. Biol.*, vol. 58, no. 16, pp. 5567–5591, Jul. 2013.

[23] J. E. Gillam, P. Solevi, J. F. Oliver, and M. Rafecas, "Simulated one-pass list-mode: an approach to on-the-fly system matrix calculation," *Phys. Med. Biol.*, vol. 58, no. 7, pp. 2377–94, Apr. 2013.

[24] A. Autret, J. Bert, O. Strauss, and D. Visvikis, "Fully 3D PET List-Mode reconstruction including an accurate detector modeling on GPU architecture," *Fully 3D 2013*, pp. 229 –232, 2013.

[25] M. Daube-Witherspoon and G. Muehllehner, "An iterative image space reconstruction algorithm suitable for volume ECT," *IEEE Trans. Med. Imaging*, vol. 5, no. 2, pp. 61–66, 1986.

[26] P. Colombino, B. Fiscella, and L. Trossi, "Study of positronium in water and ice from 22 to-144 C by annihilation quanta measurements," *Nuovo Cim. Ser. 10*, vol. 38, no. 2, 1965.

[27] G. Trumpy, "Positron annihilation in aqueous solutions," *Phys. Rev.*, vol. 118, no. 1959, pp. 668–674, 1960.

[28] K. Shibuya, E. Yoshida, F. Nishikido, T. Suzuki, T. Tsuda, N. Inadama, T. Yamaya, and H. Murayama, "Annihilation photon acollinearity in PET: volunteer and phantom FDG studies," *Phys. Med. Biol.*, vol. 52, no. 17, pp. 5249–61, Sep. 2007.

[29] Z. Liang, "Detector response restoration in image reconstruction of high resolution positron emission tomography," *IEEE Trans. Med. Imaging*, vol. 13, no. 2, pp. 314–21, Jan. 1994.

[30] D. Strul, R. B. Slates, M. Dahlbom, S. R. Cherry, and P. K. Marsden, "An improved analytical detector response function model for multilayer small-diameter PET scanners," *Phys. Med. Biol.*, vol. 48, no. 8, pp. 979–94, Apr. 2003.

[31] W. W. Moses and S. E. Derenzo, "Empirical observation for spatial resolution degradation in positron emission tomographs utilizing block detectors," *J. Nucl. Med.*, vol. 33, no. 5, p. 101P, 1993.

[32] N. Tomic, C. J. Thompson, and M. E. Casey, "Investigation of the "block effect" on spatial resolution in PET detectors," *IEEE Trans. Nucl. Sci.*, vol. 52, no. 3 I, pp. 599–605, 2005.

[33] K. Brzeziski, J. F. Oliver, J. Gillam, and M. Rafecas, "Study of a high-resolution PET system using a Silicon detector probe," *Phys. Med. Biol.*, vol. 59, no. 20, pp. 6117–6140, 2014.

[34] S. Derenzo, "Precision measurement of annihilation point spread distributions for medically important positron emitters," *5th Int. Conf. Positron Annihil.*, 1979.

[35] L. Parra and H. H. Barrett, "List-mode likelihood: EM algorithm and image quality estimation demonstrated on 2-D PET," *IEEE Trans. Med. Imaging*, vol. 17, no. 2, pp. 228–35, Apr. 1998.

[36] A. J. Reader, K. Erlandsson, M. A. Flower, and R. J. Ott, "Fast accurate iterative reconstruction for low-statistics positron volume imaging," *Phys. Med. Biol.*, vol. 43, no. 4, pp. 835–46, Apr. 1998.

[37] A. Rahmim, P. Bloomfield, S. Houle, M. Lenox, C. Michel, K. R. Buckley, T. J. Ruth, and V. Sossi, "Motion Compensation in Histogram-Mode and List-Mode EM Reconstructions: Beyond the Event-Driven Approach," *IEEE Trans. Nucl. Sci.*, vol. 51, no. 5, pp. 2588–2596, 2004.

[38] H. M. Hudson and R. S. Larkin, "Accelerated image reconstruction using ordered subsets of projection data," *IEEE Trans. Med. Imaging*, vol. 13, no. 4, pp. 601–609, 1994.

[39] D. M. Titterington, "On the Iterative Image Space Reconstruction Algorithm for ECT." *IEEE Trans. Med. Imaging*, vol. 6, no. 1, pp. 52–6, Jan. 1987.

[40] A. Reader, E. Letourneau, and J. Verhaeghe, "Generalization of the image space reconstruction algorithm," *IEEE Nucl. Sci. Symp. Conf. Rec.*, no. 6, pp. 4233–4238, 2011.

[41] G. L. Zeng and G. T. Gullberg, "Unmatched projector/backprojector pairs in an iterative reconstruction algorithm," *IEEE Trans. Med. Imaging*, vol. 19, no. 5, pp. 548–555, 2000.

[42] Y.-C. Tai, A. Ruangma, D. Rowland, S. Siegel, D. F. Newport, P. L. Chow, and R. Laforest, "Performance evaluation of the microPET Focus: a third-generation microPET scanner dedicated to animal imaging," *J. Nucl. Med.*, vol. 46, no. 3, pp. 455–63, Mar. 2005.

[43] G. Kontaxakis, L. Strauss, and G. van Kaick, "Optimized image reconstruction for emission tomography using ordered subsets, median root prior and a web-based interface," *IEEE Nucl. Sci. Symp. Conf. Rec.*, no. 1, pp. 1347–1352, 1998.

[44] J. Nuyts, "Unconstrained image reconstruction with resolution modelling does not have a unique solution," *EJNMMI Phys.*, vol. 1, no. 98, pp. 1–7, 2014.

[45] B. De Man and S. Basu, "Distance-driven projection and backprojection in three dimensions," *Phys. Med. Biol.*, vol. 49, no. 11, pp. 2463–2475, Jun. 2004.